UNIVERSITÉ LAVAL

Chip-scale, full-Stokes polarimeter

Zhongjin Lin, Leslie A. Rusch, Yuxuan Cheng, and Wei Shi

OSA Optics Express, (Volume 27, Issue 4) (2019)

https://doi.org/10.1364/OE.27.004867

© 2019 OSA. Personal use of this material is permitted. Permission from OSA must be obtained for all other uses, in any current or future media, including reprinting/republishing this material for advertising or promotional purposes, creating new collective works, for resale or redistribution to servers or lists, or reuse of any copyrighted component of this work in other works.

Copyright (c) 2019 OSA. Personal use is permitted. For any other purposes, permission must be obtained from the Optical Society of America by emailing copyright@osa.org.

Chip-scale, full-Stokes polarimeter

ZHONGJIN LIN, LESLIE RUSCH, YUXUAN CHEN, AND WEI SHI*

Department of Electrical and Computer Engineering, Center of Optics, Photonics and Laser (COPL), Université Laval, Québec, QC, Canada G1V 0A6
wei.shi@gel.ulaval.ca

Abstract: The polarization of light conveys unique information that can be exploited by crucial applications. The bulky and costly discrete optical components used in conventional polarimeters limit their broad adoption. A compact, low-cost polarimeter would bring this functionality into a myriad of new scenarios and revolutionize its exploitation. Here we present a high-performance, full-Stokes polarimeter on a silicon chip. A surface polarization splitter and on-chip optical interferometer circuit produce the complete analysis matrix of an optimally conditioned polarimeter. A matrix analysis on measurement errors is also performed. This solid-state polarimeter is a system-on-a-chip with exceptional compactness, stability, and speed that could be used singly or in integrated arrays. Large arrays can increase the speed and resolution of full-Stokes imaging; therefore, our design provides a scalable polarimeter solution.

© 2019

1. Introduction

Characterization of the state of polarization (SoP) of light is crucial for many important applications. In the field of astronomy, polarimetry can characterize the rotation of stars [1] and their stellar magnetic fields [2], which cannot be accurately measured using other properties of light. Polarimetry is also a powerful tool to characterize aerosol particles, a subject of increasing importance to both human health and our natural environment [3]. Although the earliest polarimeter dates back to the 1850s [4], state-of-the-art commercial polarimeters remain bulky, or unable to provide all four elements of the Stokes tensor, i.e., full-Stokes functionality. Recently, some miniaturized full-Stokes polarimeters have been proposed [5–8]. Capasso and co-workers designed an ultra-compact in-line polarimeter using polarization-dependent scattered fields of plasmonic metasurface [6]. Their polarimeter requires an off-chip camera to collect the scatted light, and their use of metallic nanoantennas creates parasitic absorption losses.

Silicon photonics brings to the manipulation light the economies of scale and advantages of tremendous integration long enjoyed by VLSI in electronics. Silicon photonics can integrate a vast number of optical components on a single chip in proximity with microelectronics. The manipulation of light is therefore enhanced with digital signal processing to create complete systems-on-a-chip. While silicon photonics initially targeted optical interconnects, a broader range of applications is now under development, such as sensors, light detection and ranging (LiDAR), and imaging [9]. Large-scale silicon photonic integrated circuits have been demonstrated [10–15], and are being turned to the polarimetry application. Martínez, *et al.*, used the spin-orbit interaction of light to demonstrate the use of sub-wavelength scattering on silicon for local observation of SoP [7]. They used the careful manipulation of a metallic nanoparticle or supplemental polarization filtering for their SoP characterization, however, the accuracy of their polarimeter has yet to be established with either method. A silicon photonic Stokes vector receiver has been demonstrated for high-speed optical communications [16]. It uses a nanotaper on the edge of a chip to collect light from a fiber; on-chip components such as beam splitters, polarization rotators, and optical hybrids are used for polarization decomposition and phase readouts. This structure, however, cannot be used to realize two dimensional arrays for imaging polarimetry.

In this paper, we will present a novel chip-scale, full-Stokes polarimeter in silicon photonics

National Science and Engineering Research Council of Canada (NSERC) Funding: STPGP 494358-16

Copyright (c) 2019 OSA. Personal use is permitted. For any other purposes, permission must be obtained from the Optical Society of America by emailing copyright@osa.org.

with proven SoP accuracy, compatibility with imaging polarimetry, and scalability to large arrays to enhance speed and resolution. Our polarimeter consists of a surface polarization splitter (SPS) and on-chip optical interferometers that convert the SoP directly to intensity readouts. In addition to the fiber-optic application of sensor and communication, our compact polarimeter element can be arrayed for free-space applications such as polarimetric LiDAR and imaging polarimetry. The proposed chip-scale polarimeter is based on the standard 220-nm-thick silicon-on-insulator (SOI) wafer with a 2 μm buried oxide layer and 2-μm oxide cladding.

2. Structure and principle

The schematic of the proposed device is shown in Fig. 1. A two-dimensional dielectric grating structure [17] is used as a SPS to decompose incoming light with an arbitrary SoP, (S_0, S_1, S_2, S_3), into two orthogonal linearly polarized E-field components, E_x and E_y (E_x and E_y are the complex scalars). The E-field components are separated; each has it power split (ideally a 50:50 split) and coupled into two single-mode waveguides that exit the structure in opposite directions. Note that the excited optical waves propagating in the four waveguides, $\frac{\sqrt{2}}{2}E_x$, $\frac{\sqrt{2}}{2}E_y$, $\frac{\sqrt{2}}{2}E_x$, $\frac{\sqrt{2}}{2}E_y$, carry full SoP information on the incoming light. The SoP can be retrieved using their intensities and the relative phase between the two orthogonal E-field components. Since most photo-detectors (PDs) are only sensitive to intensity, an optical interferometer circuit is designed to convert phase information into intensity. The interferometer is realized via four directional couplers (DCs).

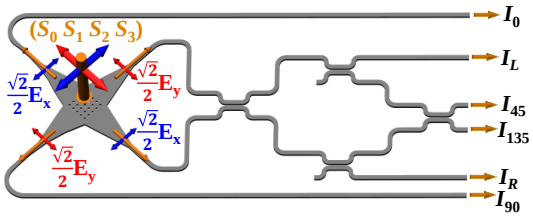

Fig. 1. A schematic of the proposed polarimeter. Incident light is decomposed into two orthogonal linear-polarization components (indicated by the blue and red arrows) that are split and coupled to four waveguides. The orange arrows point to the propagation direction of light. The outputs of the six ports are connected to photodetectors for intensity readouts: I_0, I_L, I_{45}, I_{135}, I_R, and I_{90}. Four directional couplers compose an optical interferometer circuit to calculate the third and fourth Stokes parameters.

As shown in Fig. 1, the device has six outputs. Four outputs provide intensity measurements with information on the linear polarization of incident light at specific directional rotations: linear horizontal (I_0), linear 45° (I_{45}), linear vertical (I_{90}), linear 135°(I_{135}). Two outputs provide intensity measurements with information on the circular polarization: right-handed circular (I_R), and left-handed circular (I_L) polarization.

Straight paths without directional couplers provide

$$I_0 \propto \frac{1}{2} \mid E_x \mid^2 \tag{1}$$

$$I_{90} \propto \frac{1}{2} \mid E_y \mid^2 \tag{2}$$

The interferometric structure provides

$$I_L \propto \frac{1}{8} \mid E_x e^{-i\frac{\pi}{2}} + E_y \mid^2 \tag{3}$$

National Science and Engineering Research Council of Canada (NSERC) Funding: STPGP 494358-16

Copyright (c) 2019 OSA. Personal use is permitted. For any other purposes, permission must be obtained from the Optical Society of America by emailing copyright@osa.org.

$$I_{45} \propto \frac{1}{8} \mid E_x + E_y \mid^2 \tag{4}$$

$$I_{135} \propto \frac{1}{8} \mid E_x - E_y \mid^2 \tag{5}$$

$$I_R \propto \frac{1}{8} \mid E_x + E_y e^{-i\frac{\pi}{2}} \mid^2 \tag{6}$$

We write the full-Stokes vector as $\mathbf{S} = (S_0, S_1, S_2, S_3)^T$ and the intensity vector as $\mathbf{I} = (I_0/2, I_L, I_{45}, I_{135}, I_R, I_{90}/2)^T$. The full-Stokes vector can be recovered from the six outputs via

$$\mathbf{S} \propto \mathbf{M_S} \cdot \mathbf{I} \tag{7}$$

where $\mathbf{M_S}$ is the synthesis matrix of the polarimeter, given by

$$\mathbf{M_S} = 4 * \begin{pmatrix} 1 & 0 & 0 & 0 & 0 & 1 \\ 1 & 0 & 0 & 0 & 0 & -1 \\ 0 & 0 & 1 & -1 & 0 & 0 \\ 0 & 1 & 0 & 0 & -1 & 0 \end{pmatrix} \tag{8}$$

Equation (8) is only valid under ideal conditions. Imperfections such as imbalanced splitting ratios of the SPS and DCs, waveguides losses, and phase errors should be taken into consideration. For a general expression, we rewrite the E-fields in the four waveguides coupled from the SPS as $\kappa_{x1} E_x e^{i\delta_{x1}}$,$\kappa_{x2} E_x e^{i\delta_{x2}}$, $\kappa_{y1} E_y e^{i\delta_{y1}}$, and $\kappa_{y2} E_y e^{i\delta_{y2}}$. The κ coefficients represent the impact of imbalanced splitting ratio of the SPS and waveguide losses; the δ coefficients represent the impact of phase errors. The first index refers to the E-field component (x or y), and the second index to one of the two output waveguides. The straight-through and cross-coupling coefficients of the DC are represented by τ_{DC} and κ_{DC}, respectively. A calibrated synthesis matrix $\mathbf{M'_S}$ accounting for imperfections is given by

$$\mathbf{M'_S} = 2 * \begin{pmatrix} \frac{2}{\kappa_{x1}^2} & 0 & 0 & 0 & 0 & \frac{2}{\kappa_{y1}^2} \\ \frac{2}{\kappa_{x1}^2} & 0 & 0 & 0 & 0 & -\frac{2}{\kappa_{y1}^2} \\ 0 & -a & \frac{b}{c} & \frac{-b}{c} & a & \frac{2ad\kappa_{y2}^2}{\kappa_{y1}^2} \\ 0 & b & \frac{a}{c} & \frac{-a}{c} & -b & \frac{2bd\kappa_{y2}^2}{\kappa_{y1}^2} \end{pmatrix} \tag{9}$$

where $a = \frac{\sin(\delta_{y2} - \delta_{x2})}{\tau_{DC}\kappa_{DC}\kappa_{x2}\kappa_{y2}}$, $b = \frac{\cos(\delta_{y2} - \delta_{x2})}{\tau_{DC}\kappa_{DC}\kappa_{x2}\kappa_{y2}}$, $c = 2\tau_{DC}\kappa_{DC}$, and $d = \left(\kappa_{DC}^2 - \tau_{DC}^2\right)$. In practice, the calibrated polarimetric matrix $\mathbf{M'_S}$ can be obtained by four measurements of output intensities when inputting light with known, independent SoPs.

3. Design of SPS

The schematic of SPS is shown in Fig. 2. The parameters Λ, D, and h_{etch} are the period, diameter, and etch depth of the hole, respectively. In customized CMOS-compatible silicon photonics process, the etch depth can be selected as full-etch (h_{etch} = 220 nm) or shallow-etch (h_{etch} = 70 nm). The characteristics of SPS can be controlled by Λ, D, and h_{etch}.

National Science and Engineering Research Council of Canada (NSERC) Funding: STPGP 494358-16

Copyright (c) 2019 OSA. Personal use is permitted. For any other purposes, permission must be obtained from the Optical Society of America by emailing copyright@osa.org.

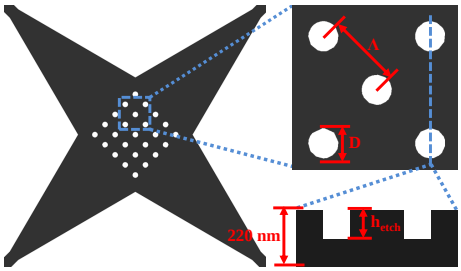

Fig. 2. Schematic of SPS. The parameters Λ, D, and h_{etch} are the period, diameter, and etch depth of the hole, respectively.

3.1. Full-etch SPS

The simulation results of full-etch SPS are given in Fig. 3. We keep the peak at 1550 nm for all of the diameters of full-etch SPS by optimizing the period. This design was focused on telecommunications wavelength band, but could be directed to the band of interest for a given application. Figures 3(b) and 3(c) show the efficiency and 3 dB bandwidth as a function of diameter. The efficiency variation does not track with variation in 3 dB bandwidth. When the full-etch SPS has high efficiency, the corresponding 3 dB bandwidth is low.

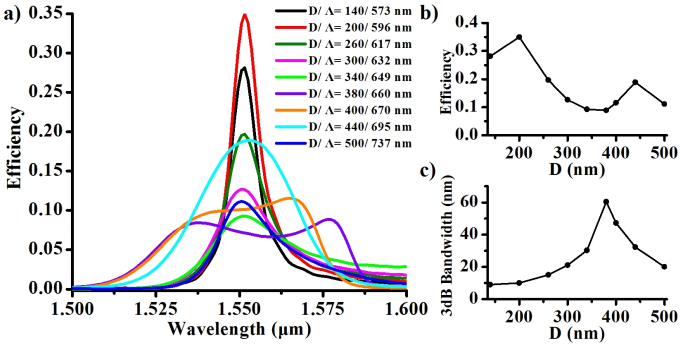

Fig. 3. Simulation results of the full-etch SPS. (a) Coupling efficiency as a function of wavelength for different diameter and period; (b) peak efficiency and (c) 3 dB bandwidth as a function of diameter.

3.2. Shallow-etch SPS

The simulation results of shallow-etch SPS are presented in Fig. 4. Figure 4(b) shows the efficiency increases with diameter. In Fig. 4(c), we observe that the 3 dB bandwidth first increases with diameter, but decreases for diameter larger than 400 nm. The shallow-etch SPS can achieve high efficiency and wide 3 dB bandwidth at the same time.

Figures 3 and 4 imply that the efficiency and bandwidth can be controlled by Λ, D, and h_{etch}. Here, we chose a full-etch SPS which Λ = 596 nm and D = 200 nm to demonstrate our device.

4. Experiment

The device was fabricated using a commercial CMOS-compatible SOI process with electron-beam lithography at Applied Nanotools Inc.. A scanning electron micrograph (SEM) of the fabricated device is presented in Fig. 5. The SPS is formed using a 20 × 20 array of cylindrical holes fully etched through silicon with a period of Λ = 596 nm and a hole diameter of D = 200 nm

National Science and Engineering Research Council of Canada (NSERC) Funding: STPGP 494358-16

Copyright (c) 2019 OSA. Personal use is permitted. For any other purposes, permission must be obtained from the Optical Society of America by emailing copyright@osa.org.

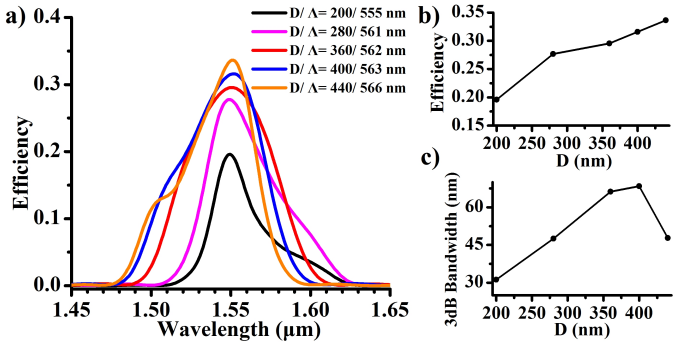

Fig. 4. Simulation results of the full-etch SPS. (a) Coupling efficiency as a function of wavelength for different diameter and period; (b) peak efficiency and (c) 3 dB bandwidth as a function of diameter.

(as shown in the inset of Fig. 5). The full-etch SPS design was adopted for the simplicity of fabrication. This design focused on the telecommunications wavelength band around 1550 nm, but could be directed to the band of interest for a given application. The conventional DC has a strong wavelength-sensitivity which would limit the bandwidth. Therefore, the broadband DC [14] will be used in our device.

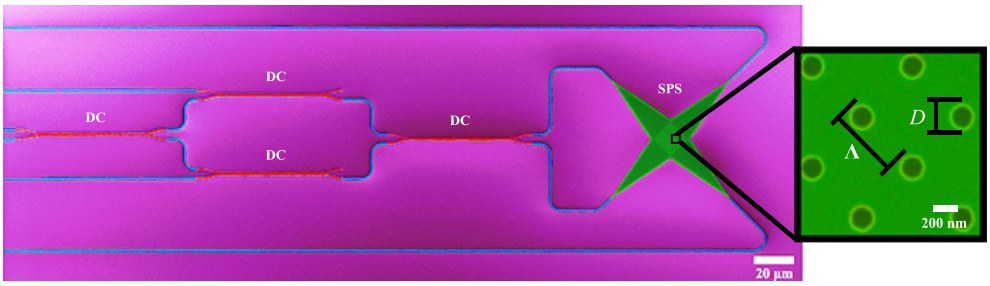

Fig. 5. SEM images of the fabricated device. The green, blue, and red areas are the surface polarization splitter (SPS), waveguides, and directional couplers, respectively. The inset shows an enlarged image of the SPS.

The experimental setup is shown in Fig. 6. Light with a wavelength of 1550 nm from a tunable laser passes through a polarization controller (PC), and then comes in and out a commercial in-line polarimeter (PSY-201-Polarization Synthesizer/Analyzer, General Photonics). Next, the light is focused on the surface of our device through Lens 1 and Lens 2 to illuminate our device with the appropriate spot size. The impact of the fiber after the in-line polarimeter has been included in the calibration matrix in our analysis. The six output ports of our device separately connect with the corresponding PDs via a fiber array, allowing us to measure the intensity at each output port of our device.

We performed the following procedure to verify that the introduction of the lens assembly did not affect the polarization of the light. The focal lengths of Lens 1 and Lens 2 are 7.5 mm and 75 mm, respectively. Their numerical apertures (NA) are 0.3 and 0.25, respectively. For an incident polarized beam, polarization aberration of a lens generates a polarization component orthogonal to the initial polarization. The extinction (i.e., the intensity ratio) of the initial polarization over its orthogonal polarization in the output is often used to characterize the polarization aberration [18]. To examine the polarization extinction of the lenses used in our experiment, we performed the test illustrated in Fig. 7(a). A linear polarization parallel to the x-axis from a PM fiber passes

National Science and Engineering Research Council of Canada (NSERC) Funding: STPGP 494358-16

Copyright (c) 2019 OSA. Personal use is permitted. For any other purposes, permission must be obtained from the Optical Society of America by emailing copyright@osa.org.

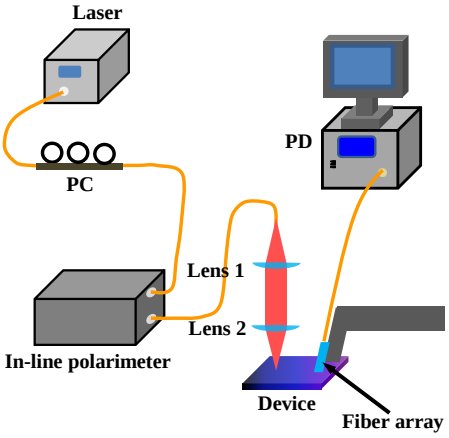

Fig. 6. Experimental Setup. Orange lines are the single mode fibers. PC is the polarization controller. PD is the photo-detector.

through the lenses and a polarizer and is then detected by a near-infrared (NIR) camera at the focal point of Lens 2. We measured the intensity profiles of the initial polarization and its orthogonal polarization through the use of a polarizer. The measured 2D intensity profiles for each (initial and orthogonal) polarization are shown in Figs. 7(b) and 7(c). Their corresponding 1D profiles across the axis illustrated in Figs. 7(b) (red line) and 7(c) (green line), respectively, are shown in Fig. 7(d). We observe that the intensity of the orthogonal polarization is below the noise floor of the camera. In the center of the focal spot, the extinction is better than 32.6 dB; it is only limited by the dynamic range of our measurement. Note that the $1/e^2$ diameter of the focal spot is ~110 μm, about nine times the size (~12 μm) of the SPS in our device (see notation in Fig. 7(d)). Therefore, the SPS only receives the center part of the focal spot where the influence of the polarization aberration of a focus lens is minimal [19]. This high polarization extinction (>32 dB) indicates that the measurement errors due to the polarization aberration of the lenses are negligible compared to other errors sources (see the section of **Appendix A** for details).

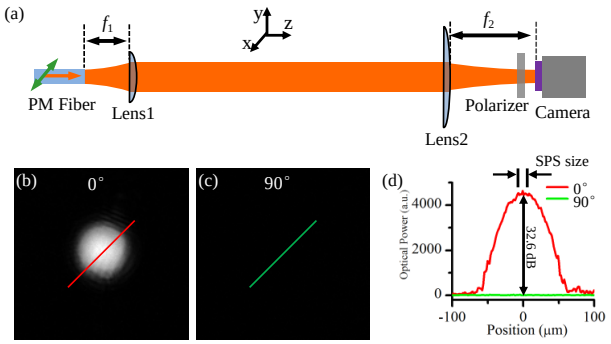

Fig. 7. Experimental Setup. Orange lines are the single mode fibers. PC is the polarization controller. PD is the photodetector.

National Science and Engineering Research Council of Canada (NSERC) Funding: STPGP 494358-16

Copyright (c) 2019 OSA. Personal use is permitted. For any other purposes, permission must be obtained from the Optical Society of America by emailing copyright@osa.org.

5. Results and discussion

The experimental and simulation results are shown in Fig. 8 when inputting (via normal incidence) x-polarized light. η_x and η_y are the efficiency of light coupled into x-directional and y-directional waveguides, respectively. The measured spectrum shows an efficiency (η_y) of near 27.7 % at the wavelength of 1550 nm. A high extinction ratio of 35 dB was measured experimentally. An image of the simulated intensity distribution withing the SPS under the x-polarized light at 1550 nm wavelength is presented in Fig. 8(b). We observe strong coupling along the vertical direction where exit paths for x-polarized component of light are located. Virtually no light is found in the horizontal direction where exit paths for y-polarized component of light are located. This is confirmed in experiment by the high extinction ratio. A better performance can be achieved using a shallow-etch desing, as shown in Section 3.

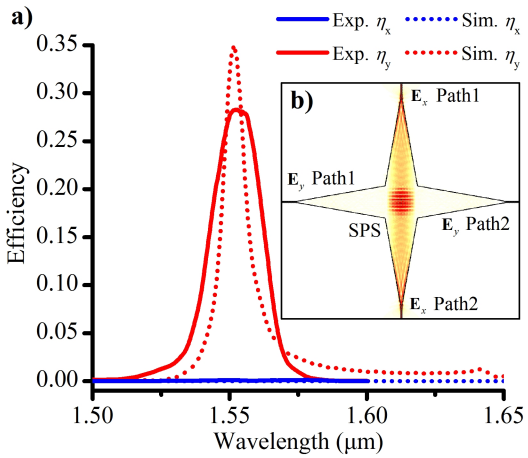

Fig. 8. Performance of the SPS. For input of x-polarized light at normal incidence, **a)** measured (solid) and simulated (dotted) coupling efficiency of light propagating in vertical waveguide (red), *i.e.*, y-direction (η_y), and horizontal waveguide (blue), *i.e.*, x-direction (η_x); **b)** The simulated intensity distributions within the SPS under the x-polarized light at 1550 nm wavelength.

Four known independent SoPs were used to calibrate the device and to calculate the system polarimetric matrix $\mathbf{M}'_{\mathbf{S}}$ (Eq. (9)). Then the performance of the polarimeter was experimentally tested using a series of SoPs spread widely over the surface of the Poincaré sphere, as illustrated in Figs. 9(a) and 9(b). For each point in this series of randomly generated SoPs, we simultaneously measured the SoP with our device and a commercial in-line polarimeter (as shown in Fig. 6). At each measurement we normalized the SoP to a unitary first component, and plotted the remaining three components, *i.e.*, $\mathbf{S}' = (S_0, S_1, S_2, S_3)^T / S_0$. The measured SoP results are summarized in Fig. 9(c). Excellent agreement is observed between the SoP measurements using our device and a commercial bench-top polarimeter. The root-mean-square error between measurements with the integrated and the bench-top instrument is 0.07. This error is dominated by intensity measurement errors due to the set-up variations and PD noise (detail shown in the **Appendix A**) [20]. This error can be significantly reduced by PDs integrated on the same chip. Notice that high-responsivity, high-speed Ge-on-Si PDs have already been demonstrated [21, 22] and are now widely available in silicon photonics foundry processes.

The condition number of the analysis matrix indicates how sensitive the reconstructed SOP is to systematic errors such as miscalibration. The signal-to-noise ratio (SNR) of a polarimeter is determined by the condition number, with SNR maximized when the condition number is

National Science and Engineering Research Council of Canada (NSERC) Funding: STPGP 494358-16

Copyright (c) 2019 OSA. Personal use is permitted. For any other purposes, permission must be obtained from the Optical Society of America by emailing copyright@osa.org.

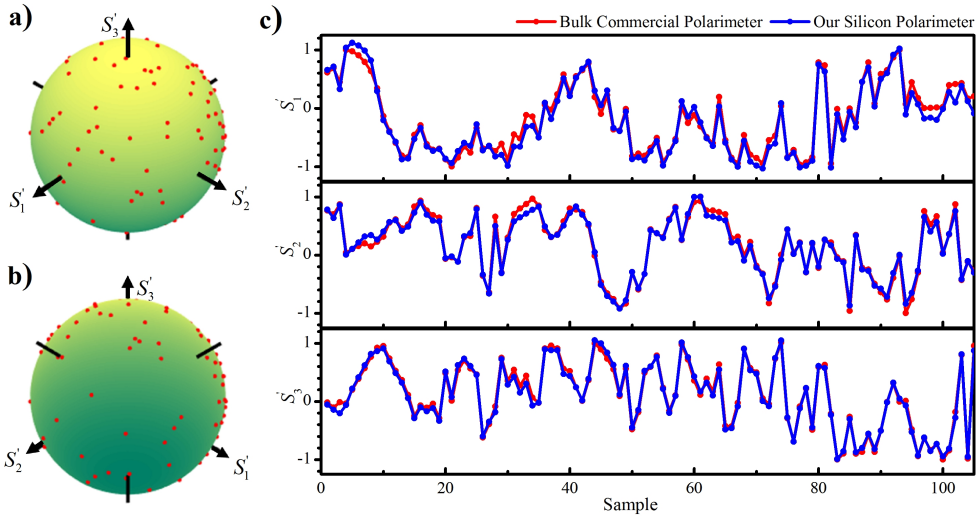

Fig. 9. Experimental results. **a)** front and **b)** back views of Poincaré sphere with red dots indicating incident polarization states dispersed randomly; **c)** measured normalized Stokes vector $\mathbf{S'} = (S_0, S_1, S_2, S_3)^T / S_0$ using our device (blue) and a commercial in-line polarimeter (red).

minimized [20]. The ideal polarimeter has a condition number of $\sqrt{3}$, the minimum value for full-Stokes analysis [20]. In addition to imperfections captured in Eq. (9), $\mathbf{M'_S}$ and its condition number is a function of wavelength due to the wavelength dependencies of the DCs and the SPS. To mitigate this effect, we used a broadband DC design with an asymmetric-waveguide-assisted section [14] leading to a more than 100 nm 1 dB bandwidth of splitting ratio (The measured and simulated results of our DC are shown in the **Appendix B**). The condition number as a function of wavelength is numerically simulated and is shown in Fig. 10. We can observe that the curve shows a flat bottom very close to the optimal value $\sqrt{3}$ across a wide spectral range from 1.5 to 1.6 μm. The condition number is also calculated using the parameters (the coupling coefficients of the DC and the extinction ratio of the SPS) extracted from measurement, and agrees well with the numerical simulation (Fig. 10).

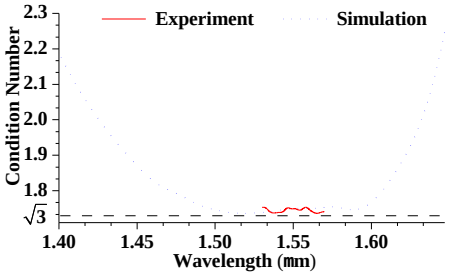

Fig. 10. The experimental and simulated condition number of the device. The red and blue line are the experimental and numerical condition number κ of the matrix $\mathbf{M'_S}$ as a function of the wavelength.

National Science and Engineering Research Council of Canada (NSERC) Funding: STPGP 494358-16

Copyright (c) 2019 OSA. Personal use is permitted. For any other purposes, permission must be obtained from the Optical Society of America by emailing copyright@osa.org.

6. Conclusion

The demonstration of a silicon full-Stokes polarimeter paves the way to polarimetry sensor systems on a chip for a vast number of applications. Avoiding the use of free-space optical and mechanical components, this solid-state solution enables significant improvement in system robustness, size and cost. A polarimeter array can also be fabricated on a single chip with minimum increase in footprint and cost, proving a scalable solution for applications such as imaging polarimetry and polarimetric LiDAR. For large-scale arrays (e.g., in 2D polarization imaging), we can spatially separate the SPS and the optical interferometer circuit, which allows us to group the SPS elements in a compact footprint to achieve a large fill factor. Furthermore, a number of the SPS elements can share one set of optical interferometer circuit and integrated PDs through on-chip optical switches [23, 24] so that the SoP received by each SPS can be analyzed in a time series. Our device can also be used as a polarization analyzer for polarimetric fiber-optic sensors whose application is limited by the high cost of currently available polarimeters. The proposed structure can be applied to other CMOS-compatible materials such as silicon nitride and germanium for a broad spectrum from visible to mid-infrared [25, 26]. Furthermore, it can be readily integrated with other silicon photonic functions such as spectrometers [27] for a multi-dimensional optical measurement system on a chip.

7. Appendix A: error analysis

In this section, we quantify the accuracy of our device and identify the major error sources. We first calibrate the polarimeter and obtain the calibrated analysis matrix $\mathbf{M}'_{\mathbf{A}}$ and the calibrated synthesis matrix $\mathbf{M}'_{\mathbf{S}}$,

$$\mathbf{I} = \mathbf{M}'_{\mathbf{A}}\mathbf{S},\ \mathbf{S} = \mathbf{M}'_{\mathbf{S}}\mathbf{I} \tag{10}$$

$\mathbf{M}'_{\mathbf{S}}$ is the general inverse matrix of $\mathbf{M}'_{\mathbf{A}}$. In the presence of various noises [19], the measured output intensity vector $\mathbf{I}'$ can be written as

$$\mathbf{I}' = (\mathbf{M}'_{\mathbf{A}} + \Delta\mathbf{M}_{\mathbf{A}})\mathbf{S} + \Delta\eta(\mathbf{M}'_{\mathbf{A}} + \Delta\mathbf{M}_{\mathbf{A}})\mathbf{S} \tag{11}$$

where $\mathbf{M}_{\mathbf{A}}$ is the deviation of the real analysis matrix of the on-chip polarimeter from the initially calibrated one (i.e., $\mathbf{M}'_{\mathbf{A}}$), $\Delta\eta$ is a 6×6 diagonal matrix representing the intensity measurement relative error (IMRE) from the test setup (such as mechanical vibration) and photodetector noises ($\Delta\eta_{ii}$ is the IMER captured by the i^{th} photodetector).

Then the reconstructed Stokes vector, $\mathbf{S}'$, can be calculated by

$$\mathbf{S}' = \mathbf{M}'_{\mathbf{S}}(\mathbf{M}'_{\mathbf{A}} + \Delta\mathbf{M}_{\mathbf{A}})\mathbf{S} + \mathbf{M}'_{\mathbf{S}}\Delta\eta(\mathbf{M}'_{\mathbf{A}} + \Delta\mathbf{M}_{\mathbf{A}})\mathbf{S} \tag{12}$$

The error of the reconstructed Stokes vector from the real value is given by

$$\Delta\mathbf{S} = \mathbf{S}' - \mathbf{S} = \mathbf{M}'_{\mathbf{S}}\Delta\mathbf{M}_{\mathbf{A}}\mathbf{S} + \mathbf{M}'_{\mathbf{S}}\Delta\eta(\mathbf{M}'_{\mathbf{A}} + \Delta\mathbf{M}_{\mathbf{A}})\mathbf{S} \tag{13}$$

The deviation ($\Delta\mathbf{M}_{\mathbf{A}}$) of the on-chip polarimeter matrix is dominated by temperature fluctuation (TF) that causes variation in the splitting ratio of the DC (i.e., κ_{DC} and τ_{DC} in Eq. (9)) and can be approximated by

$$\mathbf{M}_{\mathbf{M}ij} = \frac{\partial\mathbf{M}_{\mathbf{M}ij}}{\partial T}\Delta T \tag{14}$$

where ΔT is the temperature drift. Eqs. (13) and (14) show that TF and IMRE are the major error sources. The Monte Carlo method was used to study the influence of TF and IMRE on the root-mean-square (RMS) error of Stokes vector reconstruction. The influence of TF on the RMS error of Stokes vector reconstruction. The RMS error was calculated by generating 10^4 sudo-random polarization states and simulating the polarimeter operation with 10^3 sudo-random

National Science and Engineering Research Council of Canada (NSERC) Funding: STPGP 494358-16

Copyright (c) 2019 OSA. Personal use is permitted. For any other purposes, permission must be obtained from the Optical Society of America by emailing copyright@osa.org.

temperatures within a certain range. Fig. 11(a) shows the RMS error as a function of temperature fluctuation. We can see that the RMS error due to the temperature fluctuation is less than 10^{-5} within a variation of 10 K. In our lab, the temperature fluctuation is less than 1 K, indicating an even smaller error of less than 10^{-6}.

The RMS error originated from IMRE was calculated by generating 10^4 random polarization states and simulating the polarimeter operation with 10^3 random deviations of measured intensity. The simulated result was shown in Fig. 11(b). An about 1-dB relative error in intensity measurement was observed on our experimental setup, which gives an RMS error of 0.067, 5 orders-of-magnitude higher than that due to temperature fluctuation. This result confirms that the error (~0.07) observed in our experiment is dominated by the imperfect measurement setup.

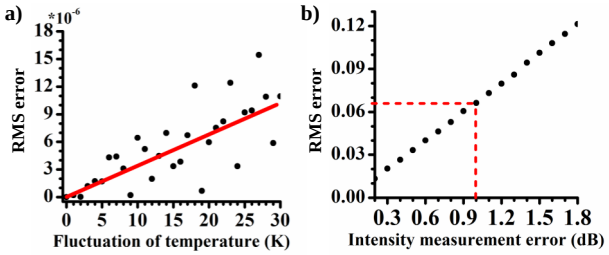

Fig. 11. Numerical results of RMS error. The simulated RMS error as a function of (a) the range of the temperature fluctuation and (b) the intensity measurement relative error (IMRE).

8. Appendix B: simulated and measured results of DC

The simulated and measured results of the DC are shown in Fig. 12, again concentrating on the telecommunications wavelength band around 1550 nm.

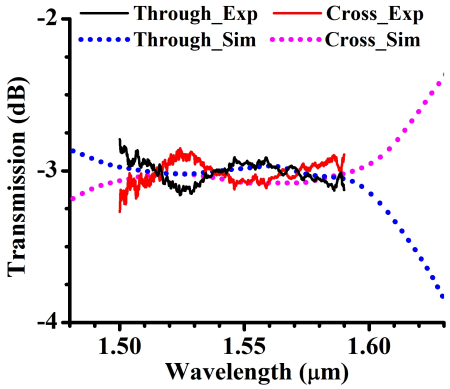

Fig. 12. Simulation and experimental results for the directional coupler (DC). Transmission in dB of straight-through (Through_Exp) and cross-coupling ports (Cross_Exp) vs. wavelength for the experiment (solid) and simulation (dotted).

Acknowledgments

This project is supported by the Natural Science and Engineering Research Council (NSERC) of Canada (STPGP 494358-16). Zhongjin Lin would like to thank the support from the China Scholarship Council (NO. 201606890030).

Copyright (c) 2019 OSA. Personal use is permitted. For any other purposes, permission must be obtained from the Optical Society of America by emailing copyright@osa.org.

References

1. D. V. Cotton, J. Bailey, I. D. Howarth, K. Bott, L. Kedziora-Chudczer, P. Lucas, and J. Hough, "Polarization due to rotational distortion in the bright star regulus," Nat. Astron. **1**, 690–696 (2017).
2. A. Chrysostomou, P. W. Lucas, and J. H. Hough, "Circular polarimetry reveals helical magnetic fields in the young stellar object HH 135–136," Nature **450**, 71–73 (2007).
3. Y.-L. Zhang and F. Cao, "Fine particulate matter (PM 2.5) in China at a city level," Sci. reports **5**, 14884 (2015).
4. G. G. Stokes *et al.*, "On the composition and resolution of streams of polarized light from different sources," Proc. Camb. Philos. **1**, 115–116 (1852).
5. P. C. Wu, J.-W. Chen, C.-W. Yin, Y.-C. Lai, T. L. Chung, C. Y. Liao, B. H. Chen, K.-W. Lee, C.-J. Chuang, C.-M. Wang, and D. P. Tsai, "Visible metasurfaces for on-chip polarimetry," ACS Photonics **5**, 2568–2573 (2017).
6. J. B. Mueller, K. Leosson, and F. Capasso, "Ultracompact metasurface in-line polarimeter," Optica **3**, 42–47 (2016).
7. A. Espinosa-Soria, F. J. Rodríguez-Fortuño, A. Griol, and A. Martínez, "On-chip optimal stokes nanopolarimetry based on spin-orbit interaction of light," Nano letters **17**, 3139–3144 (2017).
8. F. Afshinmanesh, J. S. White, W. Cai, and M. L. Brongersma, "Measurement of the polarization state of light using an integrated plasmonic polarimeter," Nanophotonics **1**, 125–129 (2012).
9. Editor, "Simply silicon," Nat. Photonics **4**, 491–491 (2010).
10. R. R. Alfano, G. Milione, E. J. Galvez, and L. Shi, "Optical sources: A laser for complex spatial modes," Nat. Photonics **10**, 286–288 (2016).
11. J. Sun, E. Timurdogan, A. Yaacobi, E. S. Hosseini, and M. R. Watts, "Large-scale nanophotonic phased array," Nature **493**, 195–199 (2013).
12. B. Shen, P. Wang, R. Polson, and R. Menon, "An integrated-nanophotonics polarization beamsplitter with 2.4× 2.4 μm 2 footprint," Nat. Photonics **9**, 378–382 (2015).
13. X. Cai, J. Wang, M. J. Strain, B. Johnson-Morris, J. Zhu, M. Sorel, J. L. O'Brien, M. G. Thompson, and S. Yu, "Integrated compact optical vortex beam emitters," Science **338**, 363–366 (2012).
14. Z. Lu, H. Yun, Y. Wang, Z. Chen, F. Zhang, N. A. Jaeger, and L. Chrostowski, "Broadband silicon photonic directional coupler using asymmetric-waveguide based phase control," Opt. express **23**, 3795–3808 (2015).
15. L.-W. Luo, N. Ophir, C. P. Chen, L. H. Gabrielli, C. B. Poitras, K. Bergmen, and M. Lipson, "WDM-compatible mode-division multiplexing on a silicon chip," Nat. communications **5**, 3069 (2014).
16. P. Dong, X. Chen, K. Kim, S. Chandrasekhar, Y.-K. Chen, and J. H. Sinsky, "128-Gb/s 100-km transmission with direct detection using silicon photonic stokes vector receiver and I/Q modulator," Opt. Express **24**, 14208–14214 (2016).
17. D. Taillaert, H. Chong, P. I. Borel, L. H. Frandsen, R. M. De La Rue, and R. Baets, "A compact two-dimensional grating coupler used as a polarization splitter," IEEE Photonics Technol. Lett. **15**, 1249–1251 (2003).
18. M. Shribak, S. Inoue, and R. Oldenbourg, "Polarization aberrations caused by differential transmission and phase shift in high-numerical-aperture lenses: theory, measurement, and rectification," in *Collected Works Of Shinya InouÉ: Microscopes, Living Cells, and Dynamic Molecules (With DVD-ROM),* (World Scientific, 2008), pp. 857–868.
19. K. Twietmeyer and R. A. Chipman, "Optimization of mueller matrix polarimeters in the presence of error sources," Opt. Express **16**, 11589–11603 (2008).
20. J. S. Tyo, "Design of optimal polarimeters: maximization of signal-to-noise ratio and minimization of systematic error," Appl. optics **41**, 619–630 (2002).
21. Y. Zhang, S. Yang, Y. Yang, M. Gould, N. Ophir, A. E.-J. Lim, G.-Q. Lo, P. Magill, K. Bergman, T. Baehr-Jones *et al.*, "A high-responsivity photodetector absent metal-germanium direct contact," Opt. express **22**, 11367–11375 (2014).
22. C. T. DeRose, D. C. Trotter, W. A. Zortman, A. L. Starbuck, M. Fisher, M. R. Watts, and P. S. Davids, "Ultra compact 45 GHz CMOS compatible germanium waveguide photodiode with low dark current," Opt. express **19**, 24897–24904 (2011).
23. T. J. Seok, N. Quack, S. Han, R. S. Muller, and M. C. Wu, "Large-scale broadband digital silicon photonic switches with vertical adiabatic couplers," Optica **3**, 64–70 (2016).
24. V. R. Almeida, C. A. Barrios, R. R. Panepucci, M. Lipson, M. A. Foster, D. G. Ouzounov, and A. L. Gaeta, "All-optical switching on a silicon chip," Opt. Lett. **29**, 2867–2869 (2004).
25. D. J. Moss, R. Morandotti, A. L. Gaeta, and M. Lipson, "New CMOS-compatible platforms based on silicon nitride and hydex for nonlinear optics," Nat. photonics **7**, 597–607 (2013).
26. R. Soref, "Mid-infrared photonics in silicon and germanium," Nat. photonics **4**, 495–497 (2010).
27. M. C. Souza, A. Grieco, N. C. Frateschi, and Y. Fainman, "Fourier transform spectrometer on silicon with thermo-optic non-linearity and dispersion correction," Nat. communications **9**, 665 (2018).

National Science and Engineering Research Council of Canada (NSERC) Funding: STPGP 494358-16